ADVANCED PHOTONICS RESEARCH Open Access
www.adpr-journal.com

Observation of Wide Bandwidth and Giant Chiroptical Response Empowered by Core–Shell Micro-Helixes

Xinggang Shang, Ning Wang, Chengyao Li, Wei Yan, Yitong Gu, Ruwen Peng, Nanjia Zhou,* and Min Qiu**

Helical microstructures exhibit unprecedented chiroptical responses particularly interesting for emerging applications such as broadband photonic components. To explore their chiral behaviors, the micro-helixes composed of polymer cores and platinum shells are proposed and realized via a two-step process combining two-photon polymerizations and sputter coating. Thanks to the core–shell multi-material configurations, the micro-helixes packed in a dense array generate an ideal chiral lineshape. Overspanning a wide range from 3 to 7 μm, the reflection-based g factors approach the upper amplitude limits. Numerical modeling reveals that polarization-induced spectra result from overlapping modes similar to the previously reported solid metal helixes. The further chiral spectrum comparisons confirm that the core–shell spirals exhibit a 25% bandwidth increase compared to solid platinum helixes of same sizes. Interestingly, the asymmetrically distributed platinum shell may further expand the operational band. Overall, comprehensive studies are performed on multi-material micro-helixes, which could provide additional flexibility to tailor their chiroptical properties, enabling the production of high-performance chiral microstructures for diverse applications.

1. Introduction

Optical chirality refers to the matter's distinct response excited by right- or left-handed circularly polarized (RCP and LCP) light.[1–3] Generating strong optical chirality with large bandwidth and enhanced amplitude would significantly profit various applications especially ones in medical and life sciences.[4–6] However, in nature, chiroptical phenomena are relatively weak due to the limited electromagnetic interaction volume.[7–9] Recent advancements in artificial micro/nanostructure[10–12] showcase substantially improved chiroptical effects, with several orders of magnitude larger than those of natural materials.[13–20] A set of chirality-related concepts have been realized and well summarized ,[21,22] with typical examples including helical chirality, chiral coupling, supramolecular chirality, pseudo chirality, and chiral scaffolds.

Among them, densely packed arrays of 3D spirals have attracted considerable attention. Since its first demonstration in 2009,[23] metal micro-helixes have been found to possess unique chiroptical properties, with both broad operational bands and great circular dichroism. Extensive investigations[24] focus on the geometric optimization of helical metamaterials, e.g., unit cell (turn, height, pitch), etc. Mainly relying on the two-photon polymerization (TPP), the varying shapes of the helixes can actively tune spectral dissymmetries to improve two key figure of merits, namely, bandwidth and extinction ratio.[24] However, research on microhelix is predominantly based on pure metallic microstructures. To further sculpture chiral–optical performance, multi-material integrated helixes should also be considered. While, due to microprocessing, current multi-material helical layouts (e.g., core–shell types with height of hundreds of nanometers) regularly

X. Shang
College of Optical Science and Engineering
Zhejiang University
Hangzhou 310027, Zhejiang, China

X. Shang, W. Yan, N. Zhou, M. Qiu
Key Laboratory of 3D Micro/Nano Fabrication and Characterization of Zhejiang Province
School of Engineering
Westlake University
Hangzhou 310024, Zhejiang, China
E-mail: zhounanjia@westlake.edu.cn; qiulab@westlake.edu.cn

The ORCID identification number(s) for the author(s) of this article can be found under https://doi.org/10.1002/adpr.202300298.

DOI: 10.1002/adpr.202300298

X. Shang, W. Yan, N. Zhou, M. Qiu
Institute of Advanced Technology
Westlake Institute for Advanced Study
Hangzhou 310024, Zhejiang, China

N. Wang, Y. Gu
Hangzhou Institute for Advanced Study
University of Chinese Academy of Sciences
Hangzhou 310024, Zhejiang, China
E-mail: wn@ucas.ac.cn

C. Li, R. Peng
National Laboratory of Solid State Microstructures
School of Physics, and Collaborative Innovation Center of Advanced Microstructures
Nanjing University
Nanjing 210023, Jiangsu, China

M. Qiu
Westlake Institute for Optoelectronics
Fuyang 311421, Hangzhou, China

work in the visible range with a limited chiral effect. To date, the explorations on multi-material composite micro-helixes are still lacking, which could be useful in expanding the design freedom and customize their chiroptical features (e.g., wider bandwidth) further.

In this report, we propose the design and manufacturing of 3D micro-helixes consisting of polymer cores and metallic shells, and experimentally demonstrate their giant chirality in the infrared regime. Compared to previous studies on micro-helix, our core–shell helix exhibits a unique near-to-upper-limit reflection-based dissymmetry factor (g factor) crossing a band from 3 to 7 μm. To construct such fine multi-material hollow objects, a two-step TPP-sputtering hybrid approach is proposed to form a conformal metallic layer on 3D polymer architectures. Subsequently, the experimental and numerical characterizations on core–shell helixes reveal that the LCP-excited photonic properties can be attributed to the modes superposition, whereas RCP fails to activate similar behaviors. The further chiral spectrum comparisons confirm that our core–shell spirals exhibit a 25% bandwidth increase compared to solid platinum helixes of same sizes. Overall, the in-depth analysis of multi-material helix optical properties unlocks key design parameters required for producing high-quality chiral structures, opening up possibilities for practical chiral–optical applications.

2. Result and Discussions

2.1. Microfabrication

The left-handed micro-helix consisting of a polymer core and a platinum shell is outlined in **Figure 1**. The overall geometry is illustrated in the schematics of Figure 1a accompanied by a top (green) and a cross-section view (yellow), respectively. The crucial structural parameters, namely, H, h, D, and d, are estimated as 5.5, 0.9, 1.1, and 0.5 μm, respectively. A hybrid process involving first TPP to print 3D helical polymer architectures, followed by sputtering of metallic layer, is developed, where the specific procedures labeled from 1 to 5 are presented in Figure 1b. Note that due to the shadow effect[25] of sputtering, the upper platinum shell should be thicker than the bottom layer (i.e., $t_2 > t_1$ in the cross section), resulting in an asymmetrically coated surface. The detailed scanning electron microscopy (SEM) image can be further checked in Figure S1, Supporting Information.

The complete manufacturing scheme starts from the photoresist (i.e., IP-Dip) dipped on a cleaned CaF_2 substrate. Employing a commercial TPP system (Nanoscribe GmbH), the polymerizations of helix prototypes could be accomplished. Subsequently, an optimized posttreatment step is adopted via a special cleaner (i.e., methyl nonafluorobutyl ether, MNE, $C_5H_3F_9O$) and violet light exposure. More discussions on this treatment can be examined in ref. [26]. Finally, the helical arrays were sputter-coated with a layer of Pt metal for shell manufacturing. Here, other types of materials could also be applied (see gold shell case in Figure S2, Supporting Information), giving an additional degree for multi-material processing and integrations.

Among these steps, the primary challenge stems from the specific helical geometries required for the generation of giant chirality, e.g., large turn numbers with a high aspect ratio.[23] Such delicate characteristics demand the precise control of the micro-fabrications. In particular, the robust polymer core lays a solid basis to bridge TPP and sputtering. Finely adjusting its strength is of vital importance to fill the gap between physical implementations and chiral functionalities. As shown in the bottom of the SEM image of Figure 1c, the polymer helixes with lower Young's module (E) cannot sustain multiple isopropanol washing, causing severe shape deformations. By contrast,

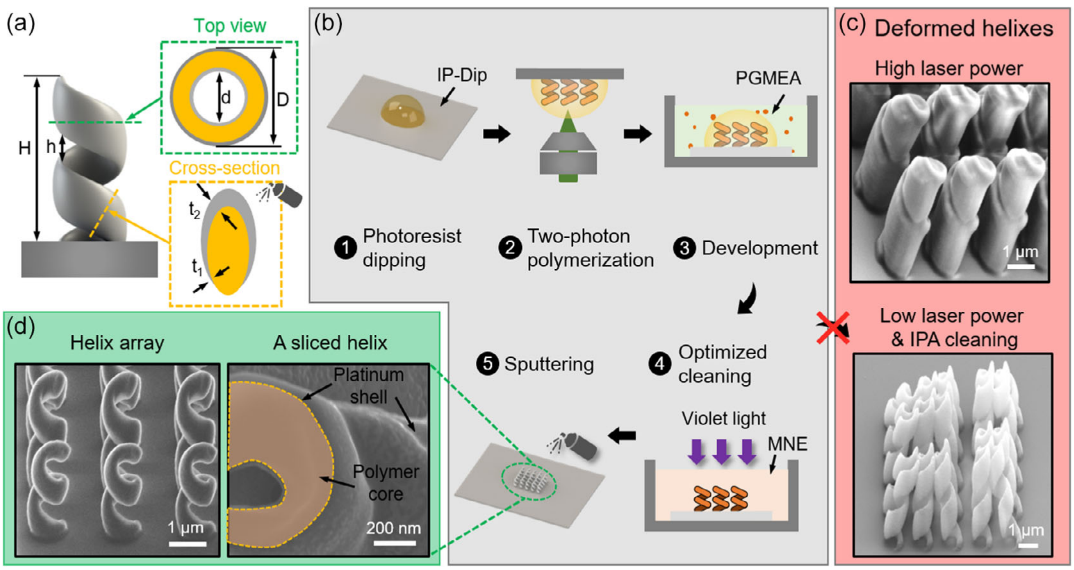

Figure 1. TPP-templated fabrications for core–shell micro-helixes. a) A schematic showing the designed helix geometry. b) Detailed manufacturing steps highlighted in the gray background. c) The scanning electron microscopy (SEM) images of defected polymer helixes that are inappropriate for later sputtering. Top: high laser power (≈20 mW), bottom: low laser power (≈10 mW) with conventional isopropanol (IPA) cleaning. d) The SEM images of a core–shell helical array (left) and a horizontally cut helix (right), respectively.

dramatically improved polymer E by increasing power would significantly reduce printing resolutions (see the upper image in Figure 1c). Hence, our improved cleaning strategy could produce sufficiently strong high-quality helixes and thus fill the gap between physical implementations and chiral functionalities. More discussions on this treatment can be examined in ref. [26].

Based on the refined TPP-sputtering method, several types of core–shell spirals have been successfully manufactured. Here, two SEM images of these samples are provided in Figure 1d. On the left, a set of identical helixes (3 × 3 objects with a pitch of 2 μm) demonstrates the fidelity of the 3D architectures. On the right, a cross-sectional view of an individual helix is revealed, where a dashed line splits the polymer core and platinum shell. The granular-like Pt distributions can be seen around the helix surfaces and on the substrate. The thickness of the metal film on the substrate is approximately 16 nm (see more details in Supporting Information).

2.2. Optical Chirality of the Core-Shell Helix

To evaluate the chirality of the proposed core–shell helix, the optical characterizations are conducted at infrared regime using a Fourier-transform infrared (FTIR) system (Vertex 70v, Bruker). The total size of the helix array is 100 × 100 μm, which covers the entire incident beam spot. **Figure 2**a shows the reflection spectra of RCP and LCP lights at normal incidence (more spectra characterizations can be seen in Figure S3, Supporting Information). There are significant reflection differences between two polarizations. The green line of R_{RCP} remains at a low value (close to zero), while LCP-induced reflections R_{LCP} exhibit a dramatic amplitude enhancement, especially at the scope from 4 to 7 μm (see more cases of oblique incidences in Supporting Information). Here, a calculated dissymmetry factor (g factor, see the orange curves) is also plotted based on two reflectances

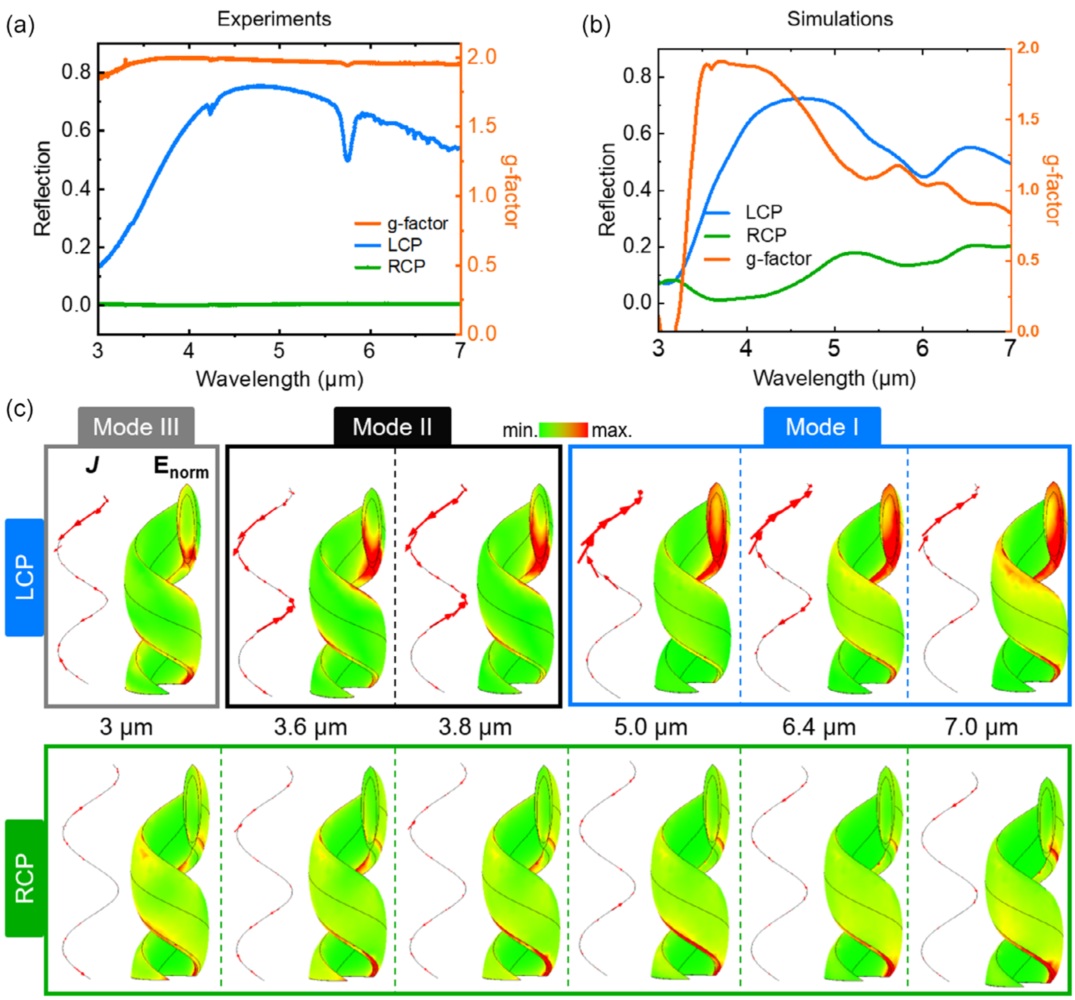

Figure 2. Optical response of helical array under LCP (blue lines) and RCP (green lines) excitations. a) Experimental and b) simulated spectra. The orange curves represent reflection-based g factors. c) Current **J** and electromagnetic fields of the core–shell helix at the corresponding wavelength (upper: LCP, lower: RCP). As wavelength increases, there exist three modes for LCP light, as highlighted in gray (Mode III), black (Mode II), and blue (Mode I) frames in the upper panel, respectively. For each wavelength, the current arrows are proportional to individual simulated data, while all E-fields of both polarizations are normalized to identical values among the whole simulated regime.

$$g_R = 2 \times \frac{R_{LCP} - R_{RCP}}{R_{LCP} + R_{RCP}} \quad (1)$$

What stands out of the g factor is the wide operating band with near-to-upper-limit amplitudes. Across the four-micrometer range (i.e., from 3 to 7 μm), the g values approach the upper bound of 2, producing an ideal lineshape of chirality.

To understand the generation of this remarkable optical response, numerical simulations employing the finite-element method are carried out. In general, the high similarities between Figure 2a,b can be noted, where the g factors are improved to a value plateau (around 1.5) within the mentioned wavelength. Concerning the value variances, many factors can be attributed, including, e.g., inaccurate modeling geometries. To be honest, it is rather difficult to precisely model the core–shell arrangement, particularly considering the asymmetrical coating. Nonetheless, the simulated results should be reliable since the major calculated spectral features match the measurements.

So far, there exist a set of studies on the resonant behavior of helix chirality. For the single isolated structure, an analytical model[23] suggests that the varied excitation efficiencies of existing modes introduce the LCP and RCP spectral differences. Regarding our densely packed array, these structures lie in a dimension between photonic crystals and effective media (i.e., the helix size approximates the same scale of pitch conditions and the operation wavelength). Under this physical scenario, earlier studies attribute the wide chiroptical features to a superposition of eigenmodes (analogous to the coupled split-ring resonators) with Bragg resonances.[23,27]

Following the previous interpretation, we first probe the disparate LCP and RCP characteristics of core–shell helixes, and then focus on the LCP circumstance, where the light polarizations agree with the helix handiness. The near-fields of LCP and RCP at 3.0, 3.6, 3.8, 5.0, 6.4, and 7.0 μm are separately plotted in the upper and lower panel of Figure 2c. At individual wavelengths, the left and right diagrams correspond to the current distributions **J** and normalized electromagnetic field (E_{norm}), respectively. Note that the **J** components perpendicular to the helical surfaces have been removed, and thereby only the **J** vectors along the helical surface are illustrated here for better visualization. More detailed descriptions could be found in Figure S4, Supporting Information.

The simulations reveal that LCP-associated spiral patterns display stronger field enhancements than RCP counterparts. In particular, the major differences manifest in the E_{norm}. The amplified E-fields of the LCP helix are mostly allocated at its head, whereas there are slight E_{norm} improvements for the RCP occasion. On the whole, the RCP helix at six wavelengths shares comparable E-field distributions. And hotspots appear near the bottom of the helix, where tiny amounts of metal are supposed to be deposited. The insufficient light–helix interactions under RCP could not trigger any effective modes.

We pay attention to the LCP cases and examine their near-fields at the relevant wavelength. Generally, we could observe three modes (see three frame labels) akin to the reported gold helix using similar sizes.[23] Three modes resemble standing waves, where the number of nodes increases from one to three as wavelength drops from 7 to 3 μm. More specifically, in the blue frame (see Mode I), the overall currents yield two standing waves (i.e., one node). The first is a dominant current **J** captured around the upper helix. This pronounced one originates from the helix center and flows toward its top. In contrast, another weaker current **J** moves to the spiral tail, generating less-visible intensities. This mode occupies a wide optical scope from 5 to 7 μm, creating an enhanced E-field at the helix head.

There are two mode transitions as wavelength decreases. The first time occurs by lowering λ from 5.0 to 3.6 μm. As expressed in mode II (see the black box), the current splits into three flows with two nodes. Primarily at 3.6 μm, three **J** parts distribute separately into the helical upper, middle, and lower sections. Here, the E-field enhancements at the head are inconspicuous compared to that of mode I. The secondary mode shift (from pattern II to pattern III) happens when the wavelength is further down to 3 μm. The gray-framed case exhibits complex current distributions in comparison to the previously discussed types. Now the current is composed of four sections. And E_{norm} is no longer concentrated at the upper turn of the helix (i.e., the weak electric field improvement can also be noticed near the helix's bottom line). All in all, the superposition of modes I, II, and III gives rise to ultrawide spectral features.

To evaluate the performance of proposed core–shell microhelixes, we have compared a set of reflective chiral structures in **Table 1**, that includes multilayer one, 2.5D stereoscopic one, metal–insulator–metal (MIM) one, and 3D helical types (this work). From the perspective of the chiral working range, our core–shell helixes reach a wide relative bandwidth (defined as Equation (2), λ_H: maximum wavelength, λ_L: minimum wavelength) of 80%, representing the best experimental value among current literature. Therefore, our design strategy provides a competitive property over all the practical attempts.

$$\mathrm{Bandwidth}_{\mathrm{relative}} = 2 \times \frac{\lambda_H - \lambda_L}{\lambda_H + \lambda_L} \quad (2)$$

Table 1. Comparisons of reflective chiral structures.

Reference	Structure	Composite materials	Bandwidth [μm]	Relative bandwidth [%]	Sim.	Exp.
[34]	Multilayered	Au-dielectric	3.8–10	89.9	✓	×
[35]	Stereoscopic	Si	9.3–10.3	10.2	✓	×
[36]	Multilayered	Au-dielectric	6–7.5	22.2	✓	✓
[37]	MIM	GST	12–14.3	17.5	✓	✓
This work	Core–shell helix	Pt-dielectric	3–7	80.0	✓	✓

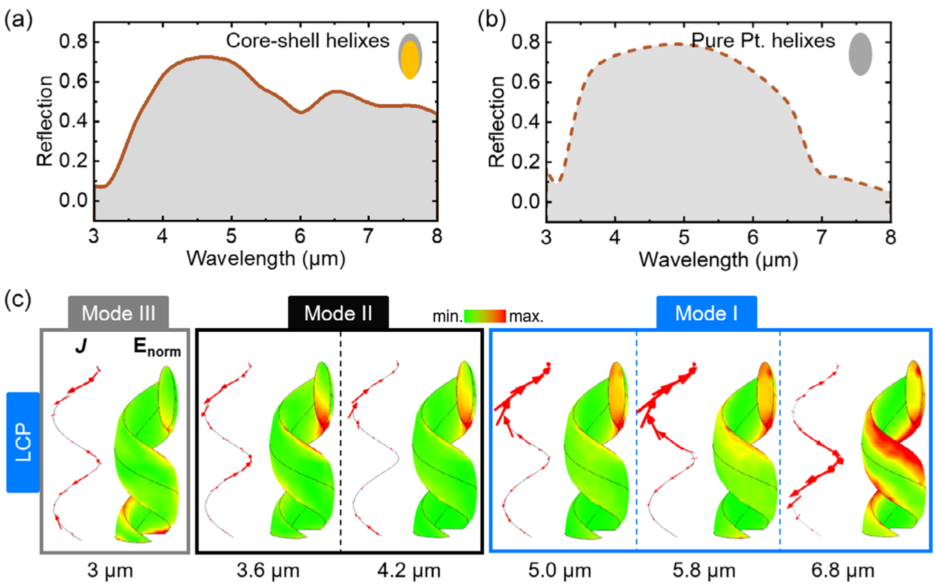

Figure 3. Simulated LCP-illuminated pure-platinum spirals and core–shell polymer-platinum ones. a,b) Reflection spectra of two types of helixes. c) Current **J** and E-fields distributions of platinum helix at the selected wavelength.

2.3. Comparative Studies Between Pure-Metal Helixes and Core–Shell Types

As shown in **Figure 3**, we further compare core–shell polymer-platinum spirals with solid platinum ones. From the following spectra, our core–shell helix displays a more than 25% wider LCP peak compared to the pure Pt kind. Similarly, we also obtain the mode overlapping for the solid spirals. As can be seen from near-field distributions, three types of modes, namely modes I, II, and III, can be indeed captured, that correspond to the previously demonstrated cases in Figure 2c, respectively.

The spectral evolutions on other types of helixes, including pure polymer core–shell and sparsely distributed ones, are presented in Figure S5 and S6, Supporting Information, respectively. Meanwhile, we also find that the asymmetrical coating may extend the full width at half maximum of g factors. In Supporting Information, we compare the core–shell helix spectra via the symmetrical and asymmetrical coated layers (see Figure S7, Supporting Information). Interestingly, the more mismatched core–shell configurations would impose a wider g factor. Regardless, this showcases an alternative way to create the ultra-broadband chiral helix. Furthermore, with the assistance of intelligence algorithms,[28] these findings may enrich new designs for specific chiroptical usages.

3. Conclusion

In conclusion, we have experimentally demonstrated core–shell polymer-platinum helixes to exhibit extraordinary chiral dissymmetry (e.g., wide bandwidth and high g factor) in the reflection spectra. An efficient fabrication method for such multi-material layouts is established utilizing TPP-created templates sputter-coated with Pt-metal layer. Subsequently, the optical characterizations reveal an ideal g-factor spectrum, where LCP light excites the high-value reflections while RCP-based amplitudes are close to zero. Corresponding numerical simulations illustrate that the LCP response is formed by mode superposition, and the core–shell asymmetrical arrangement could further benefit this response. The further comparative study manifests that the proposed core–shell spirals showcase a 25% bandwidth increase in contrast to solid platinum helixes using similar geometries. To conclude, systematic research on helix fabrications and physical properties promises chiral broadband components. This work may find numerous technological applications such as chiral detection[29–31] and sensing.[32,33]

4. Experimental Section

Fabrications: The complete manufacturing scheme started from the photoresist (i.e., IP-Dip) dipped on a cleaned CaF_2 substrate. Employing a commercial TPP system (Nanoscribe GmbH), the polymerizations of helix prototypes could be accomplished. Subsequently, an optimized post-treatment step was adopted via a special cleaner (i.e., MNE, $C_5H_3F_9O$) and violet light exposure.

Characterizations: The optical characterizations were conducted at infrared regime using an FTIR system (Vertex 70v, Bruker). The beam diameter was estimated to be around 90 μm. The total size of the helix array was 100 × 100 μm, which covered the entire incident beam spot.

Supporting Information

Supporting Information is available from the Wiley Online Library or from the author.

Acknowledgements

The authors thank Westlake Center for Micro/Nano Fabrication for the facility support and technical assistance.

Conflict of Interest

The authors declare no conflict of interest.

Author Contributions

M.Q. supervised the project. X.G.S., N.W., and M.Q. conceived the idea. X.G.S. designed and fabricated structures. C.Y.L. conducted optical characterizations. N.W. and X.G.S. performed finite element simulations and analysis. All of the authors contributed to the discussions on data analysis. The manuscript initially wrote by N.W. and X.G.S., and revised by R.W.P, N.J.Z. and M.Q.

Data Availability Statement

The data that support the findings of this study are available from the corresponding author upon reasonable request.

Keywords

chiralities, core–shell, helixes, two-photon polymerizations, wide bandwidths

Received: October 11, 2023
Revised: December 7, 2023
Published online:

[1] D. Burke, D. Henderson, *Br. J. Anaesth.* **2002**, *88*, 563.
[2] W. A. Bonner, *Orig. Life Evol. Biosph.* **1995**, *25*, 175.
[3] M. Schäferling, *Springer Ser. Opt. Sci.* **2017**, *205*, 159.
[4] P. Wittung, P. E. Nielsen, O. Buchardt, M. Egholm, B. Norde'n, *Nature* **1994**, *368*, 561.
[5] Y. Yang, R. C. Da Costa, M. J. Fuchter, A. J. Campbell, *Nat. Photonics* **2013**, *7*, 634.
[6] I. Agranat, H. Caner, J. Caldwell, *Nat. Rev. Drug Discov.* **2002**, *1*, 753.
[7] B. Yurke, A. J. Turberfield, A. P. Mills, F. C. Simmel, J. L. Neumann, *Nature* **2000**, *406*, 605.
[8] K. E. Shopsowitz, H. Qi, W. Y. Hamad, M. J. MacLachlan, *Nature* **2010**, *468*, 422.
[9] V. Sharma, M. Crne, J. O. Park, M. Srinivasarao, *Science* **2009**, *325*, 449.
[10] S. A. Maier, *Plasmonics: Fundamentals and Applications*, Springer, Berlin **2007**.
[11] B. L. Yanchuk, N. I. Zheludev, S. A. Maier, N. J. Halas, P. Nordlander, H. Giessen, C. T. Chong, *Nat. Mater.* **2010**, *9*, 707.
[12] Y. Zhao, Y. Yang, H.-B.: Sun, *PhotoniX* **2021**, *2*, 1.
[13] R. Tullius, A. S. Karimullah, M. Rodier, B. Fitzpatrick, N. Gadegaard, L. D. Barron, V. M. Rotello, G. Cooke, A. Lapthorn, M. Kadodwala, *J. Am. Chem. Soc.* **2015**, *137*, 8380.
[14] A. Y. Zhu, W. T. Chen, A. Zaidi, Y.-W. Huang, M. Khorasaninejad, V. Sanjeev, C.-W. Qiu, F. Capasso, *Light: Sci. Appl.* **2018**, *7*, 17158.
[15] W. Ma, H. Kuang, L. Xu, L. Ding, C. Xu, L. Wang, N. A. Kotov, *Nat. Commun.* **2013**, *4*, 2689.
[16] Z. Fan, A. O. Govorov, *Nano Lett.* **2010**, *10*, 2580.
[17] F. Lu, Y. Tian, M. Liu, D. Su, H. Zhang, A. O. Govorov, O. Gang, *Nano Lett.* **2013**, *13*, 3145.
[18] A. Vázquez-Guardado, D. Chanda, *Phys. Rev. Lett.* **2018**, *120*, 137601.
[19] H. Wang, Z. Qin, L. Huang, Y. Li, R. Zhao, H. Zhou, H. He, J. Zhang, S. Qu, *PhotoniX* **2022**, *3*, 1.
[20] I. Sersic, M. A. van de Haar, F. B. Arango, A. F. Koenderink, *Phys. Rev. Lett.* **2012**, *108*, 223903.
[21] V. K. Valev, J. J. Baumberg, C. Sibilia, T. Verbiest, *Adv. Mater.* **2013**, *25*, 2517.
[22] W. Jung, Y.-H. Jung, P. V. Pikhitsa, J. Feng, Y. Yang, M. Kim, H.-Y. Tsai, T. Tanaka, J. Shin, K.-Y. Kim, H. Choi, J. Rho, M. Choi, *Nature* **2021**, *592*, 54.
[23] J. K. Gansel, M. Thiel, M. S. Rill, M. Decker, K. Bade, V. Saile, G. von Freymann, S. Linden, M. Wegener, *Science* **2009**, *325*, 1513.
[24] J. Kaschke, M. Wegener, *Nanophotonics* **2016**, *5*, 510.
[25] H. Zhang, M. Liu, F. Zhou, D. Liu, G. Liu, G. Duan, W. Cai, Y. Li, *Small* **2015**, *11*, 844.
[26] X. Shang, N. Wang, Z. Wang, H. Jiang, Y. Jia, N. Zhou, M. Qiu, *Appl. Phys. Lett.* **2022**, *120*, 171107.
[27] K. Höflich, T. Feichtner, E. Hansjürgen, C. Haverkamp, H. Kollmann, C. Lienau, M. Silies, *Optica* **2019**, *6*, 1098.
[28] N. Wang, W. Yan, Y. Qu, S. Ma, S. Z. Li, M. Qiu, *PhotoniX* **2021**, *2*, 1.
[29] X.-T. Kong, L. V. Besteiro, Z. Wang, A. O. Govorov, *Adv. Mater.* **2020**, *32*, 1801790.
[30] F. Neubrech, M. Hentschel, N. Liu, *Adv. Mater.* **2020**, *32*, 1905640.
[31] J. Mun, M. Kim, Y. Yang, T. Badloe, J. Ni, Y. Chen, C.-W. Qiu, J. Rho, *Light: Sci. Appl.* **2020**, *9*, 139.
[32] E. Hendry, T. Carpy, J. Johnston, M. Popland, R. Mikhaylovskiy, A. Lapthorn, S. Kelly, L. Barron, N. Gadegaard, M. Kadodwala, *Nat. Nanotechnol.* **2010**, *5*, 783.
[33] Y. Zhao, A. N. Askarpour, L. Sun, J. Shi, X. Li, A. Alù, *Nat. Commun.* **2017**, *8*, 14180.
[34] W. Ma, F. Cheng, Y. Liu, *ACS Nano* **2018**, *12*, 6326.
[35] Y. Huang, T. Xiao, Z. Xie, J. Zheng, Y. Su, W. Chen, K. Liu, M. Tang, P. Müller-Buschbaum, L. Li, *Adv. Opt. Mater.* **2021**, *9*, 2001663.
[36] W. Ma, F. Cheng, Y. Xu, Q. Wen, Y. Liu, *Adv. Mater.* **2019**, *31*, 1901111.
[37] Y. Huang, T. Xiao, Z. Xie, J. Zheng, Y. Su, W. Chen, K. Liu, M. Tang, J. Zhu, P. Müller-Buschbaum, L. Li, *ACS Appl. Mater. Interfaces* **2021**, *13*, 45890.